Book Section:
Gandhi, B. and Dogramadzi, S. (2026) Marker density of optical tactile sensor for moving object tracking. In: Cavalcanti, A., Foster, S. and Richardson, R., (eds.) Towards Autonomous Robotic Systems. Lecture Notes in Computer Science, 16045. Springer Nature Switzerland, pp. 54-67. ISBN: 9783032014856. ISSN: 0302-9743. EISSN: 1611-3349.

https://doi.org/10.1007/978-3-032-01486-3_6

Marker Density of Optical Tactile Sensor for Moving Object Tracking

Bhoomika Gandhi[1 [0000−0002−0275−9868]] and Sanja Dogramadzi[1 [0000−0002−0009−7522]]

The University of Sheffield, England, UK
{bgandhi1,s.dogramadzi}@sheffield.ac.uk

Abstract. Soft tactile sensors have the ability to infer more physical properties of an object relative to classical optical motion-capture systems. Three marker densities in a tactile sensor array (the Motion Capture Pillow, MCP) were evaluated for tracking two rotary motions using a weighted mannequin head. The Kanade–Lucas–Tomasi algorithm was employed to track head movements using three silicone sheets, each embedded with different marker spacings (5, 10, and 15 mm). The averaged Spearman's correlation slightly changed from 0.80 (for 10 mm spacing) to 0.67 (for 5 mm spacing) for pitch motion and from 0.68 (for 10 mm spacing) to 0.59 (for 5 mm spacing) for roll motion of the mannequin head with respect to the MCP's frame. A correlation of +1.0 being the strongest positive correlation and 0.0 being weak correlation. The MAE reduced by 12.9% from matrix with 10 mm spacing to 5 mm spacing for pitch motion, and by 2.9% for roll motion. This established a foundation for further tuning the sensor using a higher density of the sensing matrix. The relatively sparsely dense sensor matrix with 15 mm spacing had minimal impact on the tracking performance of the sensor. Sources of noise were narrowed down to hysteresis, and boundary conditions. These results demonstrated the influence of marker density on the object tracking abilities of an optical soft tactile sensor, and established a basis for future optimisation.

Keywords: Motion capture · Tactile sensing · Head tracking · Spatial density

1 Introduction

1.1 Background and aim

Motion Capture via Tactile Sensing Tactile sensing in motion capture enables contact interactions with objects to obtain the physical properties, by mimicking features from the human sense of touch. This is widely used in robotics for tasks such as object manipulation, grasping, and shape recognition [17]. It does not rely on a field of view (FOV) of the target object, as seen in classical motion capture systems (e.g. VICON™), which are susceptible to errors from occlusions for such applications. Consequently, tactile sensing can provide more

information about the physical properties of an object than a non-contact optical motion capture system can, making them a valuable tool in the field of robotics and augmented/virtual reality.

Case Study The Motion Capture Pillow (MCP) [7,5] is an optical tactile sensor that is being developed to track the head movements of patients during radiotherapy for brain and head and neck (H&N) cancer treatments using the Gamma Knife® by Elekta or Linear Accelerators (LINACs). These technologies often rely on the use of thermoplastic masks for patient immobilisation which is known to cause claustrophobia among patients, and negatively affects the accuracy of the radiotherapy treatment due to patient movement arising from discomfort [6]. The sensor can improve the accuracy of the treatments by providing real-time tracking of the patient's head, while improving the potential for patient comfort.

It uses a flexible deformable silicone sheet with an array of markers embedded underneath. The deformations of these markers indicate the motion of the head in contact with the MCP via a tracking algorithm. The organisation and orientation of these markers affects the accuracy of the tracking. This paper aims to investigate the effect of varying the size of the array (i.e spacings between the markers) and builds on using the MCP with a fibrescope with greyscale image processing and Kanade-Lucas Tomasi (KLT) tracking algorithm, as was established in our previous paper [5].

1.2 Related Work

Motion capture can be achieved via contact or non-contact sensing techniques. Non-contact sensing typically uses cameras, or a marker based tracking with infrared (IR) cameras for motion tracking. Contact-based sensing methods as for example in slip detection with robotic grippers, capacitative or optical tactile sensors are commonly used for object manipulation.

Non-contact optical sensing Marker-based and markerless motion capture methods are widely used for applications in healthcare, robotics, entertainment, sports, and industrial safety measures. Although marker-based tracking provides higher accuracy over markerless systems [16,11,3], some recent developments with 3D vision cameras and deep learning algorithms for object tracking have improved the tracking accuracy of markerless vision systems to enable submillimeter accuracy. These systems overcome the limitations of marker-based tracking arising from marker occlusions since at least 4 markers are required at a point to obtain 6 DOF. An example of the markerless vision system includes markerless respiratory motion tracking for radiotherapy that used 4D deformation estimation with a mean reconstruction accuracy of ± 0.23 mm [2]. Markerless tracking has also been used in the context of MRI and PET scans using an fiber-optic camera called Tracoline 2.0 which had an average RMS motion of 5.27 mm, with a resolution of ± 0.5 mm to track respiratory movements [19]. Another commercialised approach, AlignRT™ by VisionRT [1,24] uses a markerless

approach to track surface deformations using multiple ceiling mounted cameras and provides submillimeter accuracy in 3D translational movements. Occlusion still remains an issue requiring further development in these systems, along with brightness constancy issues with markerless systems [15,12,13,28].

Soft tactile sensing Tactile sensing uses contact, which removes the restrictions related to occlusions and brightness constancy. These sensors include a range of sensors which may be capacitative, resistive, piezoelectric, thermoresistive, magnetic, or optical. Furthermore, soft tactile sensing enables non-linear deformations when interacting with objects that enables it to detect a wider range of properties such as force, object shape, slip, texture, and so on [9].

E-skins are soft flexible sensors that have been used in a variety of tactile sensing applications. For example, the eCushion [26] was designed for sitting posture monitoring. It used piezoelectric polymers to create a fabric with a 16×16 sensing grid, and obtained an accuracy of 85.9% using Naive Bayes Network based on Dynamic Time Warping used for classification. Due to the proximity of its sensing points and their structure, it suffered from inconsistency in calibration, lacked scalability due to variance in resistivity, and suffered from crosstalk. A force-sensing scalable tactile glove [20] overcame the issue of crosstalk using a custom signal isolation circuit. It was designed for object detection of a range of everyday use objects. It used conductive threads to create a knitted glove, embedded with an array of 548 piezoresistive sensors with the ability to detect 30 mN to 0.5 N each. It provided a classification accuracy of 89.4%using a ResNet-18-based architecture. A biomimetic tactile sensor, BioTAC [23], mimics the features of the human sense of touch including magnitude and direction of forces, and localising them. It used an array of electrodes embedded in a deformable finger shaped silicone elastomer. The elastomer used was Dragon Skin, along with a conductive fluid, i.e. NaCl. The electrodes were spaced 2 mm apart in a 4×5 grid. It measured the impedance variation in the conductive fluid via the embedded electrodes to estimate forces ranging from 0.1 to 30 N upon complex signal processing. The sensor suffers from hysteresis at high pressures (> 4 N). At low pressures, the spring like nature of the elastomer and the low viscosity of the conductive fluid minimised any losses from hysteresis. It also suffered from the fluid diffusing into the elastomer due to its permeability.

Optics-based soft tactile sensors have the ability to further simplify the hardware and design mechanism, since they are assisted with computer vision techniques. They primarily rely on a camera, rather than complex electronics. This also reduces their chances of crosstalk, and enables interaction with an object to infer a range of physical properties that extend beyond force applied. GelSight [29] is a high resolution tactile sensor that captures the geometry, shape and contact forces. The elastomer used is soft, clear and deformable with a reflective coating and printed patterns. RGB LED sources illuminate the cavity, allowing a camera to capture the elastomers deformations to detect the target objects' depth and orientation. The photometric stereo algorithm was used to detect forces, as low as 0.05 N with 6 DOF. HiVTac [18] also uses a similar elastomer,

called PDMS, of 500 µm which contains only 4 markers that are tracked by a camera that mimics a goniometer. It operates at a higher frequency than GelSight, at 100 Hz, enabling directional slip detection in real-time with a higher precision. It achieves a maximum error of magnitude ± 0.043N($\pm 1.547°$). Another sensor uses PDMS with an embedded fiber ring resonator to read braille. It had an accuracy of 98.5%, using an MLP neural network and 100% accuracy with an LSTM neural network [21]. The use of a 2D elastomer can be restricting when sensing depth for larger objects. DenseTact [4] is similar to GelSight but used a dome-shaped clear elastomer (Silicone Inc. P-565 Platinum Clear Silicone) with a reflective metallic ink coating (Smooth-on Psycho Paint™). The dome shape increases its depth sensing range, and enables multidirectional sensing and 3D reconstruction with a higher accuracy than GelSight. The sensor highlights an average of 0.28 mm depth difference using a neural network. TacTip [25] is also a dome-shaped sensor, similar to DenseTact. It can sense a range of object properties such as texture, slip, grip, and shape recognitions. Its dome shape is maintained by an optically clear gel called GelSight, enclosed by a 3D printed black silicone sheet (Tango Black Plus). The markers on its silicone skin are also 3D printed in a hexagonal array of 127 pins. The dimensions of the sensor are $40 \times 40 \times 85$. It uses monochrome illumination to capture the marker deformations to detect the object manipulation task using CNNs. Its small size provides a greater sensitivity to forces. The TacTip has since been developed in a range of shapes including cylinders, whiskers, and thumb [22]. Another version of TacTip improved the resolution of the sensor by using 532 pins in a geodesic pattern (with the same dimensions) [14]. This increased the object localisation accuracy of the sensor to 0.1 mm.

1.3 Contribution

The literature highlights that though marker-based systems have a higher accuracy, can be cumbersome due to limitations on the FOV. Markerless systems can overcome these limitations, however, this is at the expense of the accuracy of the tracking. Based on the related work, tactile sensors can provide more information (e.g. shape, texture, rigidity, location) about an object with a higher precision than markerless approaches. However, their accuracy based on marker density has not been thoroughly investigated, leaving a gap in the literature. In radiotherapy treatments, tactile sensors have the potential to improve the accuracy of a treatment by providing patient pose to radiographers using real-time tactile feedback.

The MCP is based on the technology behind the TacTip, where a deformable black silicone is used as the contact surface with markers embedded underneath for a camera to track the deformation of the markers. The TacTip relies on classification algorithms for interacting with a target object, rather than tracking its motion, while the MCP is being developed to track an objects' motion. The original version of the MCP [7] has a rectangular array of 19×9 markers, spaced 10 mm apart. This paper investigates the effects of the density of the sensory marker matrix on the MCP's head tracking accuracy. A mannequin based on the

weight and size of a human head was used for tracking. Metrics such as Mean Absolute Error and Spearman's correlation are used to evaluate the performance of head pose tracking.

2 Materials and Methods

2.1 Modifications in MCP design and experimental set-up

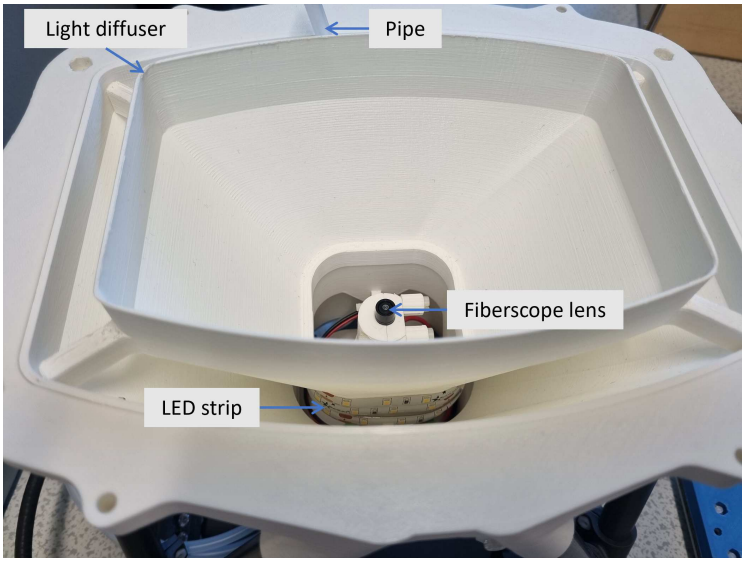

Fig. 1. The internal anatomy of the MCP. Pipe connects a PID controlled air pump mechanism to the pillow panel; LED strip illuminated the MCP to enable the camera to capture the markers on the silicone sheet via the fibrescope lens; Light diffuser minimised the light reflections captured by the fibrescope lens via the acrylic sheet.

The MCP set-up is based on a fibrescope for streaming images, and a 12V LED strip (1m long) for illumination. The internal anatomy of the MCP can be seen in Fig. 1. Three silicone sheets were created with three different spacings between the markers, 5 mm, 10 mm, and 15 mm (see Fig. 2). Non-reflective acrylic screens and a 3D printed light diffuser were used to reduce noise from the reflection of the LEDs. The diffuser blocked the LEDs directly to reduce and scatter their intensity on the acrylic sheet, and the acrylic sheets' non-reflective coating dispersed the light further to reduce the intensity of the reflections.

3D printed silicone sheets A Stratasys J750 PolyJet 3D printer was used to manufacture three silicone sheets, which are used in the pillow panels of the

MCP. Here, Agilus 30 was used for the black silicone, and VeroWhite Plus for the embedded white markers.

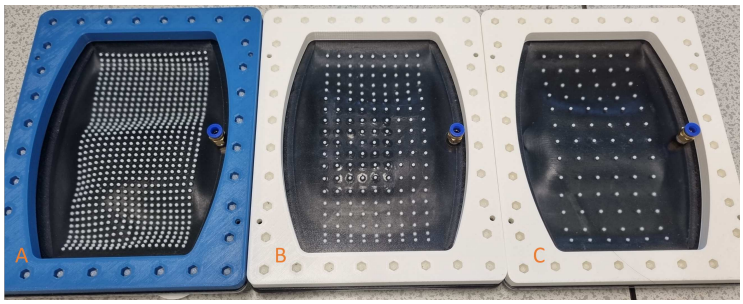

Fig. 2. Three pillow panels with varying spacings in their silicone sheets: A. 5 mm spacing (38 × 19), B. 10 mm spacing (19 × 9), and C. 15 mm spacing (13 × 6), with non-reflective acrylic sheets.

Hardware Set-Up A weighted 3D printed mannequin head of 3 kg was used to test the three sensing matrices of the MCP, since this is the lowest average human head weight [27], with the Franka Emika Panda robot arm for manipulation. The mannequin head manipulation involved its rotation in the x (roll) and y (pitch) axes of the MCP's frame, F_P. Custom attachments for the end-effector of the robot arm were also 3D printed using tough Polylactide (PLA) to secure the mannequin head. See Fig. 3 for the experimental set-up used for data collection. The air pressure in the pillow panels was set at 1.7 kPa using a PID controller. This maintains the pillow's concave shape and provides patient-comfort. A detailed explanation of this mechanism is described in our previous paper [5], the reader is encouraged to read it for a better understanding of the hardware set-up. For brevity, this is not repeated here.

2.2 Data Collection

The robot arm performs two motions on the mannequin, pitch and roll, respective to the MCP's frame, F_P. The pitch motion rotates the mannequin head by 20° each side from the home position (which is set to 0°), around the y-axis of F_P. Here, one cycle consists of four rotations in total since it starts from the home position, rotates 20°clockwise and anti-clockwise, followed by a further anti-clockwise and clockwise rotation by the same magnitude. The roll motion rotates it 7° in an anti-clockwise direction around the x-axis of F_P, followed by a clockwise rotation back to its home position, consisting of two rotations in total in one cycle. The end-effector pose data was recorded to provide ground truth, and the fibrescope in the MCP streamed the images at the same frequency along with the pressure sensor measuring the values inside the pillow panel. All

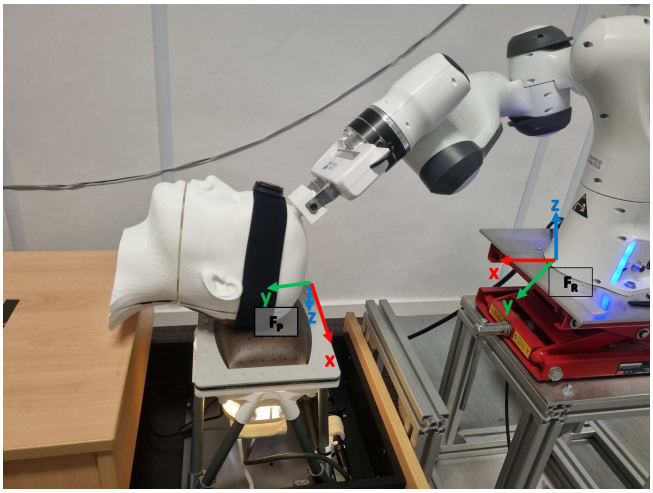

Fig. 3. Experimental set-up of MCP, Franka Emika Panda robot arm, and 3D printed weighted mannequin head in home position. F_P stands for frame of the pillow (MCP), and F_R for robots' base frame.

the data were collected synchronously at a sampling frequency of 10 Hz, and five recordings were taken for each motion (5 pitch rotation and 12 roll rotation cycles) using each pillow panel. The set-up used for this was the same as a previous study [5].

2.3 Data Analysis

KLT tracking algorithm The KLT algorithm based on Shi-Tomasi corner detector was utilised for data analysis. The maximum corners parameter for this was modified to 300, 100, and 50, for the marker matrix spacings 5, 10, and 15 mm respectively, to effectively detect all the markers on the three different sensing arrays. These parameters were determined by trial and error, ensuring all the markers were being covered. Here, the maximum corners for the panel with 10 mm spacing was kept the same as in the previous work [5].

Spearman's correlation This metric calculates the correlation between two one-dimensional continuous numeric datasets, and is adaptable to non-linear data [8]. Here, the experimental values from the MCP were compared against the ground truth values from the robot arm. The correlation factor ranges from -1 to 1, where correlations close to zero signify poor correlation while correlations closer to 1 or -1 demonstrate a strong positive or negative correlation, respectively. This measure was used to establish a proof of how related the two variables are, using eq. (1).

$$\rho = 1 - \frac{6 \sum d_i^2}{n(n^2 - 1)} \tag{1}$$

Here ρ is the Spearman's correlation coefficient, d_i is the difference between two ranks of each observation, and n is the number of observations.

Mean Absolute Error (MAE) This is a commonly used measure to obtain an average of the errors in the predicted values, compared to the ground truth. It is calculated in the same units as the target variable, simplifying its interpretation [10]. It was calculated using eq. (2). A small error signifies good prediction, whereas a larger error signifies vice versa.

$$MAE = \frac{1}{N}\sum_{i=1}^{N}|y_i - x_i| \tag{2}$$

Here, y_i is the prediction from the MCP, and x_i is the ground truth from the robot arm.

Hysteresis This was examined by splitting the motion cycles into loading and unloading phases for one trial and averaging them to obtain a mean loading and unloading curve. In the loading phase, the mannequin head moves away from its home position (at 0°), while in the unloading phase, it moves back to the home position. The pitch motion was divided into four parts with one loading and unloading on each of the two sides (left and right sides of the home position), while the roll motion was divided into two parts (up and down) for loading and unloading.

3 Results

The results were obtained based on the KLT algorithm, using Spearman's correlation and MAE, both relative to the ground truth from the robot arm. The silicone sheet with 5 mm marker spacing has the lowest correlation with the ground truth for both, pitch and roll motions, along with the lowest yet most precise MAE score (minimum variation between samples) for roll with a mean of 1.34° for the five samples. The pitch motion data from the 5 mm sheet shows consistent noise at the maximum range of the motion, approximately above 9° in Fig. 6, so it was calculated again by adding a threshold to eliminate any motion beyond 9°. Upon the removal of this noise, the MAE average for the trials changed from 12.88° to 4.99°. For the same sheet the roll motion predictions remain consistent with a relatively higher precision than the other sheets, as is seen in Fig. 4.

The silicone sheets with 10 mm and 15 mm spacings show similar results to each other, signifying that reducing the density of the markers does not necessarily improve or reduce the performance of the MCP, but a higher density with 5 mm spacing can improve the performance.

The predictions from the MCP were in pixels and were scaled to the range of motion as established via the ground truth during post processing. A sample of the raw signals can be seen in Fig. 5.

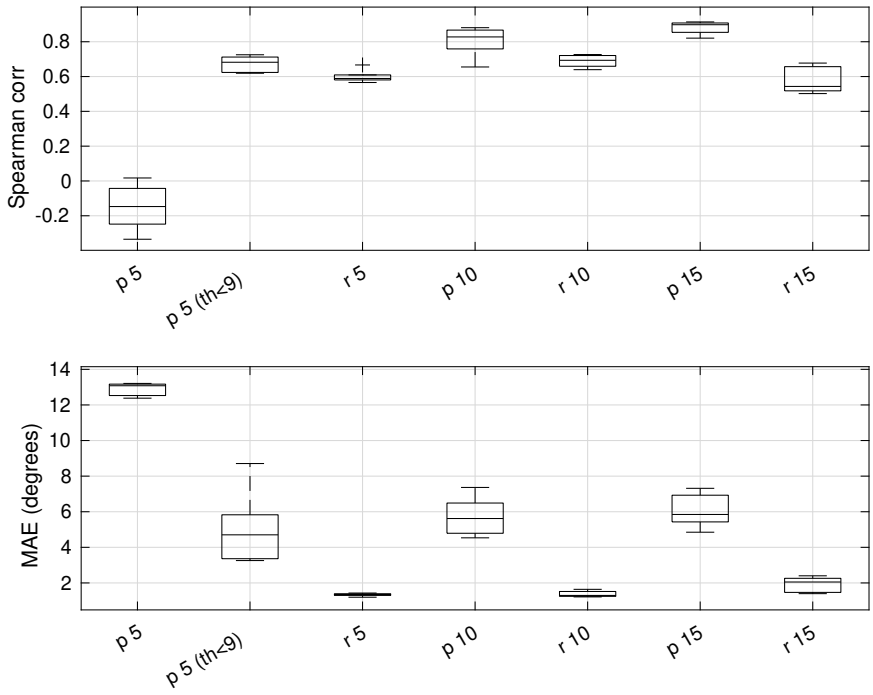

Fig. 4. Spearman's Correlation for the two rotational motions, pitch (p) and roll (r) of the mannequin for all three marker spacings - 5 mm, 10 mm and 15 mm, and Mean Absolute Error (MAE) in degrees for the same. Here, th refers to threshold, which was set to 9°and the other values were ignored for this calculation.

Spearman's correlation was also used to compare the results from the three pillow panels. Since the 10 mm spacing has been used in previous works, the correlations of the silicone sheets were calculated relative to this, see Fig. 7, where it shows roll motion from the 15 mm sheet with maximum correlation, followed by pitch from the 15 mm sheet. This is consistent with the previous results where the two sheets, 10 mm and 15 mm spacings show an insignificant difference. Roll from 5 mm shows a relatively lower correlation, and pitch from 5 mm shows the lowest correlation.

The hysteresis plots generated for the three marker densities for each motion can be seen in Fig. 8 and Fig. 9. These results show a slight lag in the MCP predictions relative to the ground truth data, with some discrepancy between the loading and unloading curves.

For pitch motion with 5 mm spaced markers, the maximum MCP predictions are approximately 10°. This is related to the consistent noise, which was also reflected in its low spearman correlation and the raw data. This noise is also seen in the hysteresis plot in Fig. 8.

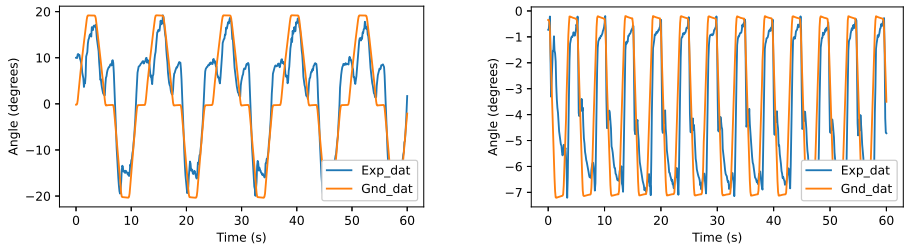

Fig. 5. A sample of pitch (left) and roll (right) motions from the silicone sheets with 10 mm marker spacing, with MCP predictions showing a consistent overshoot at 0° for pitch motion.

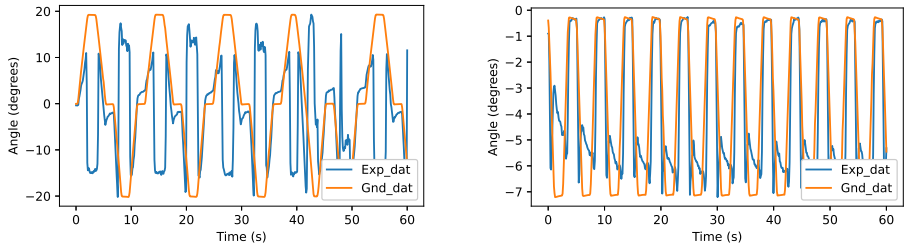

Fig. 6. A sample of pitch (left) and roll (right) motions from the silicone sheets with 5 mm marker spacing, showing more noise in pitch than roll motion.

4 Discussion

The results obtained from the three silicone sheets were as expected for the pitch motion, with the 5 mm marker spacing being an exception. This has noise induced at the extreme ends of the motion which could be due to a significant amount of markers that were being tracked leaving the FOV of the camera. The MAE for this was significantly improved when a threshold was set to consider head rotation angles below 9°. This demonstrates that a higher density of the marker matrix can provide more accuracy, although further testing is required upon improving the FOV of the sensor. These results are similar to the TacTip Superresolution model which had a higher marker density than the first TacTip, resulting in a higher accuracy [14]. To reach the maximal performance from this marker array, the sensor's design requires modifications to increase the distance between the camera lens and the silicone sheet to ensure a thorough coverage of all markers.

The spearman's correlation was strong (> 0.6) for all of the motions and sensor densities, except for the boundaries of the silicone sheet with 5 mm spacing. This correlation metric cannot be used to establish a direct relationship between the MCP predictions and the ground truth, further work is required to obtain this using kalman filtering.

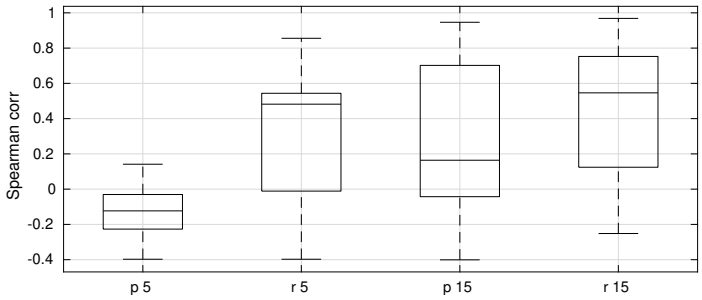

Fig. 7. Cross correlation between the silicone sheets with 5 mm and 15 mm spacing, with respect to 10 mm spacing for pitch, p, and roll, r, motions.

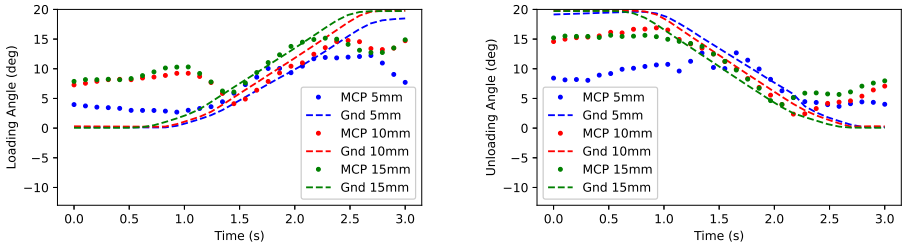

Fig. 8. Loading (left) and unloading (right) for pitch motion for the three silicone sheets with varying sensing matrix density, showing an average of the loading and unloading cycles from one trial.

The hysteresis graphs show the averaged loading and unloading phases for trials, providing more clarity to the raw data signals. The pitch motion shows similar trends for 10 mm and 15 mm spacing, but 5 mm spacing shows lower loading values at the initial resting stage and lower peak resting values. This solidified that the data from this sensor matrix was more consistent when the motion was below 9° where the sensor matrix was accurately captured by the camera. The roll motion had a smaller range, hence showed consistent results for the three sensing matrices. The MCP predictions show a stronger lag here than in the pitch motion. This could be due to larger air pressure variations within the MCP as the centre of mass of the mannequin head shifts along with the mannequin during the motion. Unloading had a larger lag than loading, which was due to hysteresis in the silicone used in the MCP. The effects of this could be reduced with slower loading and unloading with longer wait times between the two phases. Furthermore, using thinner silicone sheets with relatively lower pressure as seen in [23], or using chemical grafting such as polypyrrole on a porous PDMS substrate can reduce the effects of hysteresis further [17].

The noise in the pitch motion was more disruptive than the noise in the roll motion, which may be due to the range of motion being larger and the motion having more steps along the trajectory causing uneven pressure changes in the

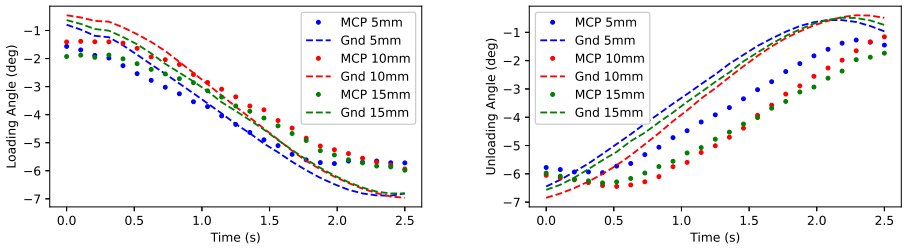

Fig. 9. Loading (left) and unloading (right) for **roll** motion for the three silicone sheets with varying sensing matrix density, showing an average of the loading and unloading cycles from one trial.

MCP. When it reached 0° in the pitch motion, the air pressure differences caused a small spike and a delay in the estimations stabilising again. This was not an issue with the roll motion since it was a more consistent motion.

5 Conclusion and future work

The MCP is a contact-based optical tactile sensor, that uses an array of markers. The optimal density of these markers has been evaluated in this work by comparing three spacing parameters (5 mm, 10 mm, and 15 mm) for the sensing matrix embedded in the silicone sheets of the pillow panels. This was used for tracking the motion of a 3D printed weighted mannequin head for two rotatory motions - pitch and roll with respect to F_P.

It shows that a higher density of the sensing matrix in the optical tactile sensor can improve the accuracy of the head tracking for rotational motions in the pitch and roll axes of F_P. This was established using performance metrics such as Spearman's correlation and MAE. Sources of noise in the data are due to hysteresis, air pressure changes in the MCP, and background noise, which require further processing to filter through. These results create a solid foundation to further investigate the relationship between the KLT values from the dense sensing matrix and the head poses.

Future works also involve testing the MCP in a participant study to make it more versatile to the variations in human motions and the variations in their head types (e.g. weight, shape, and hair type); along with improving the robustness of the sensor with sensor fusion techniques using a gyroscope.

Acknowledgment

We are grateful to the EPSRC providing funding the PhD research of the first author of this work (Grant number: 2607213). This work was also supported by the Henry Royce Institute for Advanced Materials, funded through EPSRC grants EP/R00661X/1, EP/P025021/1 and EP/S019367/1.

References

1. AlignRT® Advance - Vision RT — visionrt.com. https://www.visionrt.com/alignrtadvance/, [Accessed 01-Jun-2022]
2. Berkels, B., Bauer, S., Ettl, S., Arold, O., Hornegger, J., Rumpf, M.: Joint surface reconstruction and 4d deformation estimation from sparse data and prior knowledge for marker-less respiratory motion tracking. Medical Physics **40**(9), 091703 (2013)
3. Das, K., de Paula Oliveira, T., Newell, J.: Comparison of markerless and marker-based motion capture systems using 95% functional limits of agreement in a linear mixed-effects modelling framework. Scientific Reports **13**(1), 22880 (2023)
4. Do, W.K., Kennedy, M.: Densetact: Optical tactile sensor for dense shape reconstruction. In: 2022 International Conference on Robotics and Automation (ICRA). pp. 6188–6194. IEEE (2022)
5. Gandhi, B., Mihaylova, L., Dogramadzi, S.: Head tracking using an optical soft tactile sensing surface. Frontiers in Robotics and AI **11**, 1410858 (2024)
6. Goldsworthy, S., McNair, H., Dogramadzi, S.: Motion capture pillow (mcp): A novel method to improve comfort and accuracy in radiotherapy. Clinical Medicine **19**(Suppl 2), 103 (2019)
7. Griffiths, G., Cross, P., Goldsworthy, S., Winstone, B., Dogramadzi, S.: Motion capture pillow for head-and-neck cancer radiotherapy treatment. In: 2018 7th IEEE International Conference on Biomedical Robotics and Biomechatronics (Biorob). pp. 813–818. IEEE (2018)
8. Hauke, J., Kossowski, T.: Comparison of values of pearson's and spearman's correlation coefficients on the same sets of data. Quaestiones geographicae **30**(2), 87–93 (2011)
9. Hughes, J., Culha, U., Giardina, F., Guenther, F., Rosendo, A., Iida, F.: Soft manipulators and grippers: A review. Frontiers in Robotics and AI **3**, 69 (2016)
10. Hyndman, R.J., Koehler, A.B.: Another look at measures of forecast accuracy. International journal of forecasting **22**(4), 679–688 (2006)
11. Kanko, R.M., Laende, E.K., Davis, E.M., Selbie, W.S., Deluzio, K.J.: Concurrent assessment of gait kinematics using marker-based and markerless motion capture. Journal of biomechanics **127**, 110665 (2021)
12. Le Moing, G., Ponce, J., Schmid, C.: Dense optical tracking: Connecting the dots. In: Proceedings of the IEEE/CVF Conference on Computer Vision and Pattern Recognition. pp. 19187–19197 (2024)
13. Lee, B.Y., Liew, L.H., Cheah, W.S., Wang, Y.C.: Occlusion handling in videos object tracking: A survey. In: IOP conference series: earth and environmental science. vol. 18, p. 012020. IOP Publishing (2014)
14. Lepora, N.F., Ward-Cherrier, B.: Superresolution with an optical tactile sensor. In: 2015 IEEE/RSJ International Conference on Intelligent Robots and Systems (IROS). pp. 2686–2691. IEEE (2015)
15. Li, K., He, F.Z., Yu, H.P.: Robust visual tracking based on convolutional features with illumination and occlusion handing. Journal of Computer Science and Technology **33**, 223–236 (2018)
16. Puthenveetil, S.C., Daphalapurkar, C.P., Zhu, W., Leu, M.C., Liu, X.F., Chang, A.M., Gilpin-Mcminn, J.K., Wu, P.H., Snodgrass, S.D.: Comparison of marker-based and marker-less systems for low-cost human motion capture. In: International Design Engineering Technical Conferences and Computers and Information in Engineering Conference. vol. 55867, p. V02BT02A036. American Society of Mechanical Engineers (2013)

17. Pyo, S., Lee, J., Bae, K., Sim, S., Kim, J.: Recent progress in flexible tactile sensors for human-interactive systems: from sensors to advanced applications. Advanced Materials **33**(47), 2005902 (2021)
18. Quan, S., Liang, X., Zhu, H., Hirano, M., Yamakawa, Y.: Hivtac: A high-speed vision-based tactile sensor for precise and real-time force reconstruction with fewer markers. Sensors **22**(11), 4196 (2022)
19. Slipsager, J.M., Ellegaard, A.H., Glimberg, S.L., Paulsen, R.R., Tisdall, M.D., Wighton, P., Van Der Kouwe, A., Marner, L., Henriksen, O.M., Law, I., et al.: Markerless motion tracking and correction for pet, mri, and simultaneous pet/mri. Plos one **14**(4), e0215524 (2019)
20. Sundaram, S., Kellnhofer, P., Li, Y., Zhu, J.Y., Torralba, A., Matusik, W.: Learning the signatures of the human grasp using a scalable tactile glove. Nature **569**(7758), 698–702 (2019)
21. Wang, H., Ma, L., Nie, Q., Hu, X., Li, X., Min, R., Wang, Z.: Optical tactile sensor based on a flexible optical fiber ring resonator for intelligent braille recognition. Optics Express **33**(2), 2512–2528 (2025)
22. Ward-Cherrier, B., Pestell, N., Cramphorn, L., Winstone, B., Giannaccini, M.E., Rossiter, J., Lepora, N.F.: The tactip family: Soft optical tactile sensors with 3d-printed biomimetic morphologies. Soft robotics **5**(2), 216–227 (2018)
23. Wettels, N., Santos, V.J., Johansson, R.S., Loeb, G.E.: Biomimetic tactile sensor array. Advanced robotics **22**(8), 829–849 (2008)
24. Wiersma, R.D., Tomarken, S., Grelewicz, Z., Belcher, A.H., Kang, H.: Spatial and temporal performance of 3d optical surface imaging for real-time head position tracking. Medical physics **40**(11), 111712 (2013)
25. Winstone, B., Griffiths, G., Melhuish, C., Pipe, T., Rossiter, J.: Tactip—tactile fingertip device, challenges in reduction of size to ready for robot hand integration. In: 2012 IEEE International Conference on Robotics and Biomimetics (ROBIO). pp. 160–166. IEEE (2012)
26. Xu, W., Huang, M.C., Amini, N., He, L., Sarrafzadeh, M.: ecushion: A textile pressure sensor array design and calibration for sitting posture analysis. IEEE Sensors Journal **13**(10), 3926–3934 (2013)
27. Yoganandan, N., Pintar, F.A., Zhang, J., Baisden, J.L.: Physical properties of the human head: mass, center of gravity and moment of inertia. Journal of biomechanics **42**(9), 1177–1192 (2009)
28. Yu, J.J., Harley, A.W., Derpanis, K.G.: Back to basics: Unsupervised learning of optical flow via brightness constancy and motion smoothness. In: Computer Vision–ECCV 2016 Workshops: Amsterdam, The Netherlands, October 8-10 and 15-16, 2016, Proceedings, Part III 14. pp. 3–10. Springer (2016)
29. Yuan, W., Dong, S., Adelson, E.H.: Gelsight: High-resolution robot tactile sensors for estimating geometry and force. Sensors **17**(12), 2762 (2017)